NASA Technical Memorandum 106933
IECEC–95–136

Analysis of Solar Receiver Flux Distributions for US/Russian Solar Dynamic System Demonstration on the MIR Space Station

Thomas W. Kerslake and James Fincannon
Lewis Research Center
Cleveland, Ohio

Prepared for the
30th Intersociety Energy Conversion Engineering Conference
cosponsored by ASME, IEEE, AICHE, ANS, ACS, and AIAA
Orlando, Florida, July 31–August 1, 1995

National Aeronautics and
Space Administration

ANALYSIS OF SOLAR RECEIVER FLUX DISTRIBUTIONS FOR US/RUSSIAN SOLAR DYNAMIC SYSTEM DEMONSTRATION ON THE MIR SPACE STATION

Thomas W. Kerslake
James Fincannon
NASA Lewis Research Center
21000 Brookpark Road, MS 500-203
Cleveland, Ohio 44135

ABSTRACT

The United States and Russia have agreed to jointly develop a solar dynamic (SD) system for flight demonstration on the Russian MIR space station starting in late 1997. Two important components of this SD system are the solar concentrator and heat receiver provided by Russia and the U.S., respectively. This paper describes optical analysis of the concentrator and solar flux predictions on target receiver surfaces. The optical analysis is performed using the code CIRCE2. These analyses account for finite sun size with limb darkening, concentrator surface slope and position errors, concentrator petal thermal deformation, gaps between petals, and the shading effect of the receiver support struts. The receiver spatial flux distributions are then combined with concentrator shadowing predictions. Geometric shadowing patterns are traced from the concentrator to the target receiver surfaces. These patterns vary with time depending on the chosen MIR flight attitude and orbital mechanics of the MIR spacecraft. The resulting predictions provide spatial and temporal receiver flux distributions for any specified mission profile. The impact these flux distributions have on receiver design and control of the Brayton engine are discussed.

INTRODUCTION

The United States and Russia have agreed to jointly develop a solar dynamic (SD) system for flight demonstration on the Russian MIR space station starting in late 1997 (see Figure 1). The U.S. government-contractor team is providing the heat receiver, closed Brayton cycle power conversion equipment, National Space Transportation System (NSTS) certification and launch to the MIR space station. The Russian government-contractor team is providing the solar concentrator, heat rejection system, pointing and tracking system, ground integration of system hardware, and on-orbit hardware integration and operation on MIR. Information about this program is given by Wanhainen and Tyburski (1995).

The solar concentrator has 36 individually deployable reflective petals that form an on-axis paraboloid. The paraboloid has a 3.7 m focal length, a 2 m inner diameter and a 9.5 m outer diameter. To meet system thermal input power requirements, the concentrator has a mirrored surface of approximately 5 m which provides a 37° rim angle. A cylindrical, cavity-type heat receiver is located at the concentrator focal plane. The cavity is lined with heat exchanger tubes which store thermal energy and heat the working fluid (see Figure 2). A 0.24 m diameter circular aperture is centered at one end of the receiver cavity to admit concentrated solar energy. Energy not intercepted by the aperture is deposited on a segmented graphite aperture shield designed to protect the underlying metal structure from excessive temperatures. Three steel c-channel support struts, 0.127 m wide by 0.063 m deep, connect the receiver to the base of the concentrator. The receiver design is described in detail by Strumpf et al (1995).

To enable receiver thermal stress analyses, solar flux distributions must be calculated for the receiver cavity and aperture shield. This paper describes analyses conducted to determine these distributions. The analyses account for a finite sun size with limb darkening, concentrator surface slope and position errors, concentrator petal thermal deformation, gaps between petals, and the shading effect of the receiver support struts. The receiver spatial flux distributions are then combined with concentrator shadowing predictions from the code OSSA (Orbiting Spacecraft Shadowing Analysis) developed by NASA Lewis Research Center (Fincannon, 1995). Geometric shadowing patterns are traced from the concentrator to the target receiver surfaces. These patterns vary with time depending on the chosen MIR flight attitude and orbital mechanics of the MIR spacecraft. The resulting predictions provide spatial and temporal receiver flux distributions for any specified mission profile.

ANALYSIS

Concentrator Optical Modeling

The concentrator was modeled as a single parabolic facet and analyzed with the code CIRCE2 developed by Sandia National Laboratory (Romero, 1994). The CIRCE2 code is based on cone

optics theory and has been verified with experimental data (Grossman et al., 1992). The small gaps between concentrator petals result in a projected area loss between 1% and 3%. To account for this area loss, the solar insolation (1415 W/m^2) incident on the concentrator was reduced by 3%. Based on a grid sensitivity study, the concentrator parabolic facet was discretized into 372 subfacets with approximately equal radial and meridional dimensions. The distribution of reflected energy is calculated for each subfacet.

The concentrator surface inaccuracy was modeled in two ways. First, a one-dimensional Gaussian distribution of overall surface "slope error" with a 6.8 mrad standard deviation was employed. The "slope error" accounts for not only petal reflective surface imperfections but also for petal thermal deformation, position error, material outgassing error, and acceleration error. Second, the thermal deformation component was removed from the overall slope error creating a Gaussian distribution with 2.4 mrad standard deviation. The petal contour with thermal deformation was calculated separately (based on initial petal thermal vacuum optical tests) and used directly as input into CIRCE2. With the expected thermal loading, the mirrored surface temperature will be greater than the back surface temperature causing the petal to flatten and increasing petal effective focal length. Of the two methods for modeling surface inaccuracies, the latter is consistent with test data and is believed to be more representative of concentrator behavior in the low Earth orbit thermal environment.

A standard sun limb darkening model was employed to describe the sun shape, i.e. the solar intensity versus solid angle. Since the concentrator RMS slope error is 2 to 3 times the RMS value for typical sun shape models, target flux distributions are not sensitive to assumed sun shape. The incident sun shape and concentrator error cone, both modeled as one-dimensional circular-normal distributions, were convolved analytically at a single incidence angle (angle between principal incident solar ray and the ideal facet surface normal). Based on test data, a beginning-of-life specular reflectance of 0.83 was assigned to the SiO_2-coated aluminum reflective surface.

Target Geometries

The receiver cavity target surface was defined as a cylinder 0.483 m in diameter and 0.762 m in length. The surface was discretized circumferentially into 15.6° angular segments (one for each of 23 receiver tubes). The surface was discretized into 0.0254 m segments along the length which correspond to the positions of individual phase change material thermal energy storage (TES) canisters located concentrically around each receiver tube. The cavity aperture plane is positioned coincident with the concentrator focal plane.

The receiver aperture plane target surface was defined by a 1 m diameter, flat circular disk located in the concentrator focal plane. The surface was discretized into 0.01 m radial increments. Solar energy incident on the target at a radius less than 0.12 m would be intercepted by the receiver aperture.

Concentrator Shadowing

Figure 3 shows the geometric solid model of the MIR space station as it will appear in late 1997 with the SD system attached to the Krystall module. Given this geometry model, articulating surface rotation angles (i.e. tracking data), Sun pointing angle and MIR attitude, the OSSA code calculates the shadow patterns on the concentrator throughout the orbit. Shadowing predictions were generated for two typical MIR flight modes: solar inertial, where the MIR attitude does not change as viewed from the Sun, and Earth inertial, where the MIR attitude continually changes throughout the orbit as viewed from the Sun. The former results in a static concentrator shadow pattern while the latter causes a transient shadow pattern.

The concentrator grid pattern for shadow calculations was selected by geometrically tracing individual receiver cavity tube and TES canister positions back to the concentrator segment providing illumination. Cavity back wall segments corresponding with receiver tubes were also traced back to the concentrator. This allows for a one-to-one mapping of flux level and shadowing condition to the target surface. The concentrator shadowing grid and shadowing results are given by Fincannon (1995).

The struts supporting the receiver produce a constant shading pattern within the receiver cavity. The struts were sized and positioned to completely shade three tubes within the receiver. For these analyses, tube numbers 1, 8 and 17 were permanently shaded by struts. The three struts block 14% of the solar energy reflected toward the receiver aperture.

DISCUSSION OF RESULTS

Cavity Fluxes Without Shadowing

Figure 4 shows the unshadowed incident solar flux on the receiver cavity for the cases of Gaussian and non-Gaussian (separate) petal thermal deformation. In both cases, the intercepted power level is just under 14 kW. The receiver tube inlet end starts at a position 0.146 m behind the concentrator focal plane while the tube outlet end is located 0.762 m behind the focal plane. The non-Gaussian concentrator modeling has two primary effects: (1) increasing the peak flux from 2.7 W/cm^2 to 3.7 W/cm^2 and (2) shifting the location of peak flux 0.1 m toward the rear of the cavity. The sharp, non-Gaussian flux distribution is a result of the relatively small effective petal slope error. The rear shifting of incident energy is due to petal thermal flattening which translates the effective concentrator focal plane inside the receiver cavity.

In comparison to the Gaussian flux distribution, the non-Gaussian distribution has several deleterious impacts on receiver thermal-structural performance and on the Brayton engine thermodynamic performance. The higher incident flux levels lead to higher TES canister absorbed fluxes, higher temperature gradients and higher thermal stresses. The rear-shifted flux reduces direct illumination of TES canisters located in the front of the receiver cavity. Therefore, the TES canisters in the rear of the cavity attain higher temperatures and must store more energy by cycling through a greater temperature range over an orbit. Also, receiver tube temperatures are increased in order to transfer heat to the warmer working fluid near the tube exit. With higher illuminated tube temperatures, the temperature difference between shadowed and

unshadowed tubes increases. This temperature difference is the primary cause of thermal stresses in receiver tubes and manifolds. A detailed account of receiver thermal stress performance is given by Strumpf (1995).

The greater orbital temperature range of rearward TES canisters also leads to a greater orbital variation in receiver working fluid outlet temperature (equal to the engine turbine inlet temperature (T6A)). Since the maximum T6A must be limited to achieve acceptable turbine scroll operating life, the orbit-averaged T6A must decrease with the non-Gaussian receiver flux distribution. This, in turn, decreases the engine electric output power proportionally with T6A (for a given turbine speed and pressure ratio).

Cavity Fluxes With Shadowing

Figure 5 shows a sequence of cavity incident flux distributions with a non-Gaussian concentrator model and concentrator shadowing from a typical MIR Earth inertial flight mode. For this case, MIR is in a 400 km circular orbit inclined 51.6° with a 20° solar beta angle (angle between the orbit plane and solar vector). Flux levels are shown versus distance behind the focal plane and versus receiver tube number in the cavity circumferential direction.

The concentrator is not shadowed for up to 10 minutes past orbit sunrise. Figure 5a, 15 minutes past sunrise, shows that about half of the cavity is shadowed (between tube numbers 2-6 and 16-23). Maximum shadowing occurs 19 minutes past sunrise (see Figure 5b) and reduces the receiver intercept power to 26% of the unshadowed value. At 24 minutes past sunrise, Figure 5c, shadowed regions have diminished and cover about half the receiver tubes. At 36 minutes past sunrise, the receiver cavity returns to an unshadowed condition for the remainder of the 57-minute sun period. The resulting sun time averaged intercept power was 11 kW or 80% of the unshadowed intercept power. For this case, the transient shadow pattern resulted from the Kvant-2 module and its two pairs of solar array wings passing in front of the concentrator. Concentrator shadow pattern predictions are discussed by Fincannon (1995).

Cavity flux distributions with similar appearance were predicted for MIR solar inertial flight modes. These distributions remain fixed throughout the orbit sun period. Static cavity shadow patterns with sharp boundaries between adjacent tubes create large temperature differences. This tube temperature difference drives receiver tube and manifold thermal stresses. Compared to solar inertial shadowing cases, receiver tube and manifold thermal stress are generally more benign for Earth inertial shadow cases. This is a result of TES canister thermal mass reducing tube temperature transients.

The engine controller must be capable of adjusting turbine speed consistent with receiver thermal input for a wide range of shadowing conditions. This capability is required to maintain engine temperatures and pressures within design operating limits. Relatively slow changes in shadowing conditions occur day-to-day as orbit parameters vary. Such changes are predictable. However, rapid shadowing changes are possible in consecutive orbits if MIR maneuvers to different flight attitudes. These changes are not known a prior since detailed MIR mission operations plans are not finalized until two weeks prior to execution. Therefore, the controller must be designed to accommodate worst case orbit-to-orbit shadowing changes.

Aperture Plane Fluxes

Figure 6 shows cross-sectional aperture plane flux distributions with Gaussian and non-Gaussian concentrator modeling. Both cases assume no concentrator shadowing and no concentrator pointing error. The Gaussian distribution has a peak flux of 88 W/cm^2 centered in the circular aperture and a 9 W/cm^2 flux level at the aperture edge (0.12 m radius). The non-Gaussian distribution has a 96 W/cm^2 peak flux at a 0.03 m radius and an aperture edge flux of 1 W/cm^2. The multi-lobe character of this distribution is due to concentrator petal thermal flattening which has shifted the focal plane behind the receiver aperture plane.

Figure 7 shows the Gaussian and non-Gaussian aperture plane flux distributions with a 4.5° concentrator pointing error. For certain MIR or SD system emergencies, the concentrator will be off-pointed and maintained at a 4.5° pointing error until complete concentrator off-pointing can take place during orbit eclipse. This emergency pointing mode ensures that concentrated solar flux impinges on the receiver graphite aperture shield. This minimizes the risk of illuminating MIR station hardware with high fluxes and interrupts receiver thermal input to allow SD system shutdown. The Gaussian distribution in Figure 7a shows only a small maximum flux level reduction (from 88 W/cm^2 to 78 W/cm^2) due to off-pointing and shows little aperture plane image dispersion.

By contrast, the off-pointed non-Gaussian maximum flux has increased to 165 W/cm^2 (from 96 W/cm^2) and the aperture plane image is significantly spreading on the image leading edge along the direction of off-pointing (positive Y-axis). This behavior with increasing off-point angle is the result of competing factors: image dispersion and solar ray reflector-target path length changes. As the image disperses, flux levels decrease. Flux levels increase, however, from initial increases in solar ray path lengths that better align the thermally deformed concentrator focal plane with the aperture shield target surface. At an off-point angle of 5°, the concentrator average path length increase roughly equals the increase in effective focal length of thermally deformed petals. For off-pointing angles greater than 5°, path length increases start to defocus the concentrator and flux levels fall off. Decreases in solar ray path length also defocus the concentrator and decrease flux levels. Figure 8 illustrates the net effect of these competing factors on aperture plane peak flux and radial location versus off-point angle. The maximum predicted incident flux is 165 W/cm^2. At this flux level, the adiabatic gray-body equilibrium temperature is greater than 2300 K. This temperature level clearly dictates the use of graphite for constructing the passively cooled aperture shield segments.

SUMMARY AND CONCLUDING REMARKS

To support development of the MIR SD flight demonstration, optical analyses of concentrator-receiver system were performed. Analysis results were combined with concentrator shadowing

predictions to define receiver flux distributions. These distributions are being used to design the receiver and Brayton cycle engine hardware. These distributions have also proved useful in SD system analyses to define acceptable system start-up and operating envelopes.

More refined optical analyses are planned for the coming year when as-built, concentrator petal thermal and optical properties are measured. Concentrator modeling will include individual petal optical characteristics (reflectance, slope error distribution, and thermally deformed shape) and petal deployment position.

ACKNOWLEDGEMENT

The authors wish to thank Mr. Jeff Hojnicki of NASA Lewis Research Center for writing the postscript plotting code needed to produce the flux contour plots.

REFERENCES

Fincannon, J., 1995, "Analysis of Shadowing Effects on MIR Photovoltaic and Solar Dynamic Power Systems," *Proceedings, 30th Intersociety Energy Conversion Engineering Conference*, Orlando, Florida.

Grossman, J. W., et al., 1987, "Prototype Dish Testing and Analysis at Sandia National Laboratory," *Proceedings, 1992 ASME-JSES-KSES International Solar Energy Conference*, Maui, Hawaii.

Romero, V. J., 1994, "CIRCE2/DEKGEN2: A Software Package for Facilitated Optical Analysis of 3-D Distributed Solar Energy Concentrators," Sandia National Laboratory, SAND91-2238.

Strumpf, H. J., et al., 1995, "Heat Receiver For Joint US/Russian Solar Dynamic Flight Demonstration Project," *Proceedings, 30th Intersociety Energy Conversion Engineering Conference*, Orlando, Florida.

Wanhainen, J. S. and Tyburski, T. E., 1995, "Joint US/Russian Solar Dynamic Flight Demonstration Project Plan," *Proceedings, 30th Intersociety Energy Conversion Engineering Conference*, Orlando, Florida.

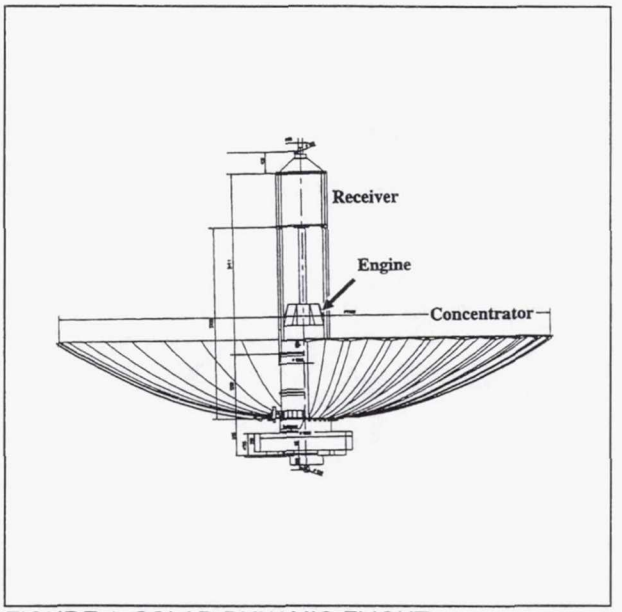

FIGURE 1. SOLAR DYNAMIC FLIGHT DEMONSTRATION HARDWARE

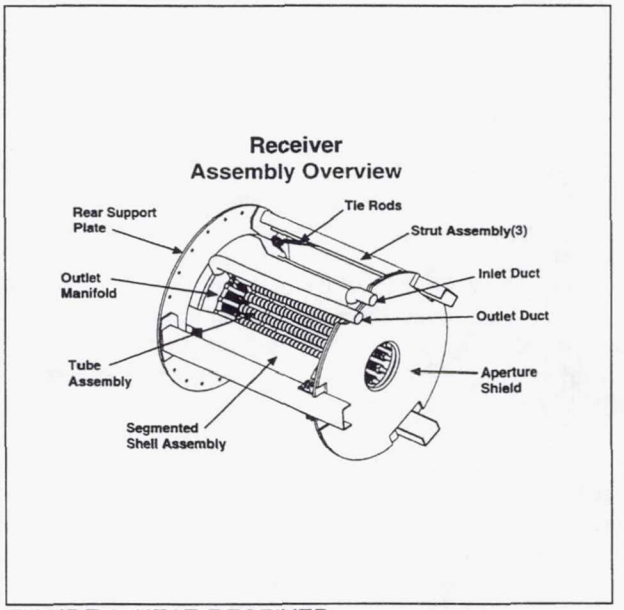

FIGURE 2. HEAT RECEIVER

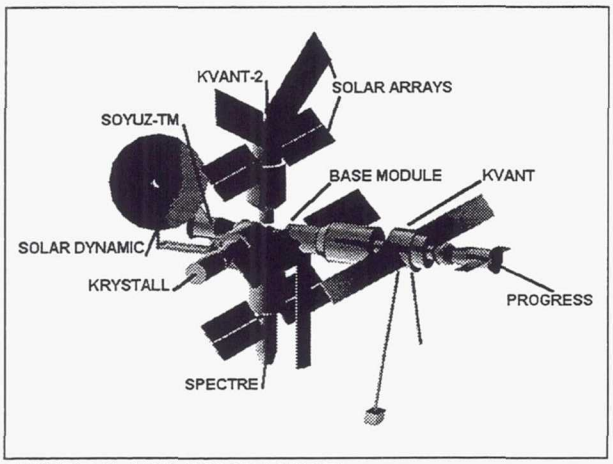

FIGURE 3. MIR SOLID MODEL

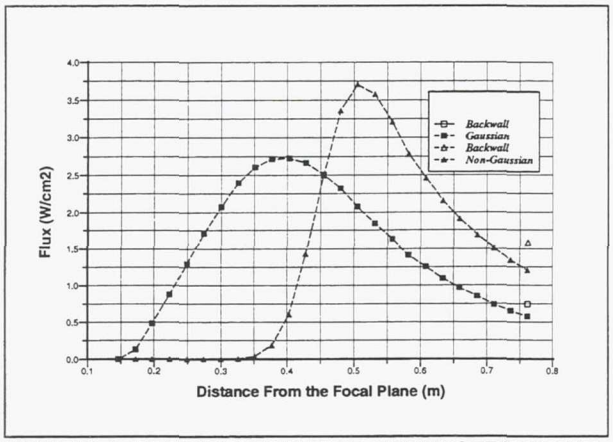

FIGURE 4. RECEIVER CAVITY FLUX DISTRIBUTION

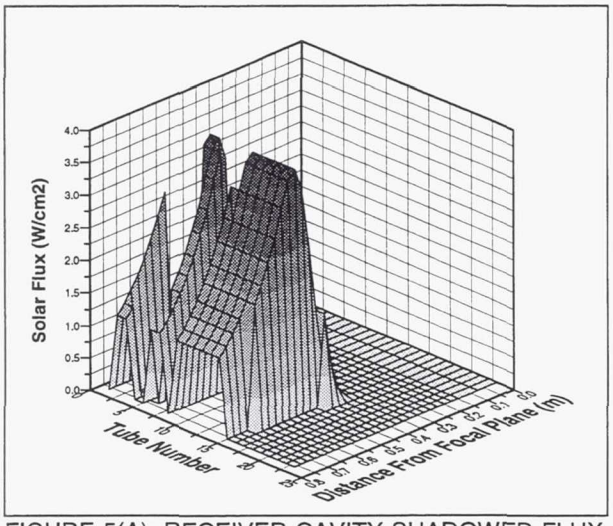

FIGURE 5(A). RECEIVER CAVITY SHADOWED FLUX DISTRIBUTION AT TIME = 15.36 MIN.

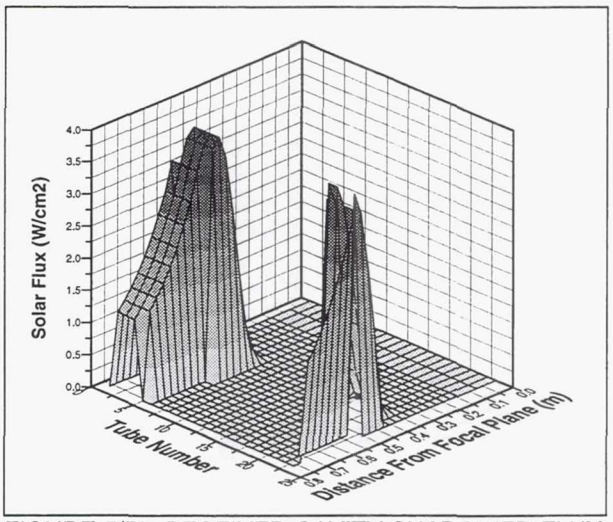

FIGURE 5(B). RECEIVER CAVITY SHADOWED FLUX DISTRIBUTION AT TIME = 19.45 MIN.

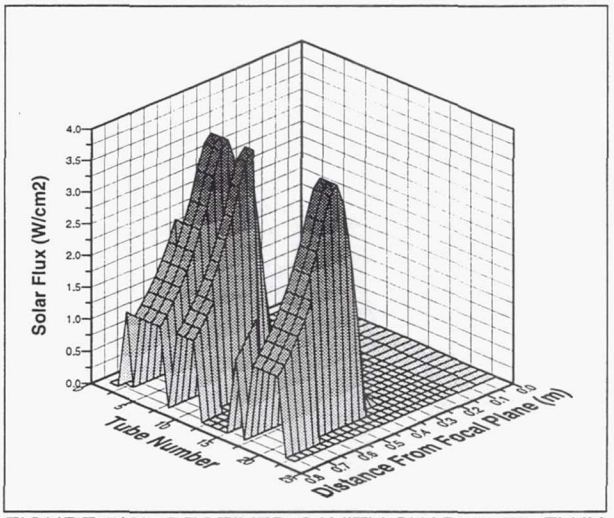

FIGURE 5(C). RECEIVER CAVITY SHADOWED FLUX DISTRIBUTION AT TIME = 24.57 MIN.

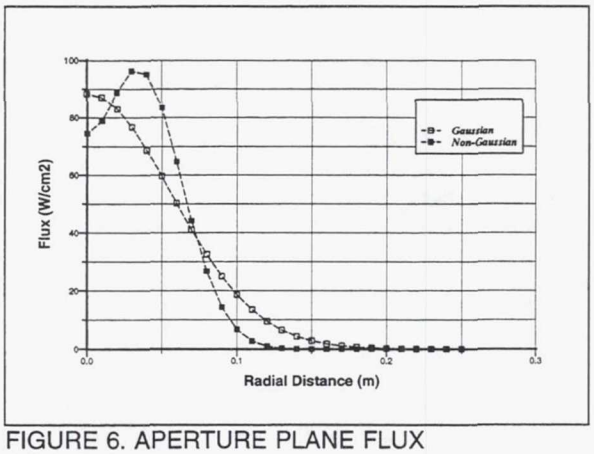

FIGURE 6. APERTURE PLANE FLUX DISTRIBUTION

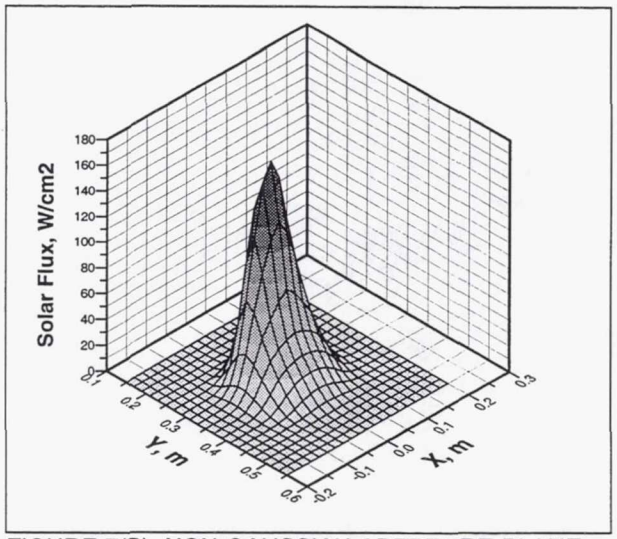

FIGURE 7(B). NON-GAUSSIAN APERTURE PLANE FLUX DISTRIBUTION WITH 4.5 DEG POINTING ERROR (APERTURE CENTER AT X=Y=0)

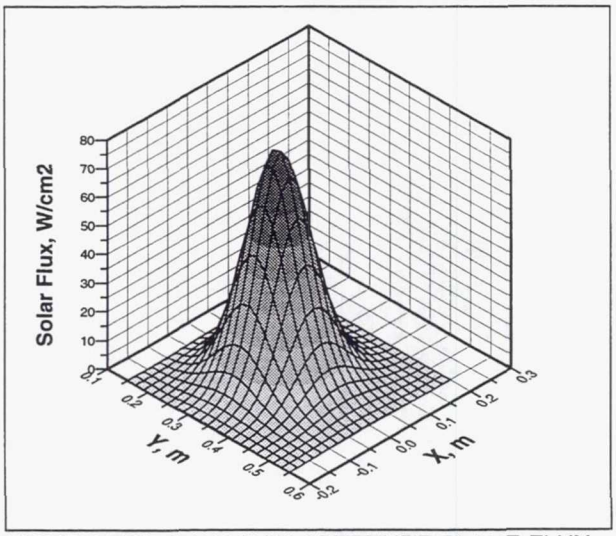

FIGURE 7(A). GAUSSIAN APERTURE PLANE FLUX DISTRIBUTION WITH 4.5 DEG POINTING ERROR (APERTURE CENTER AT X=Y=0)

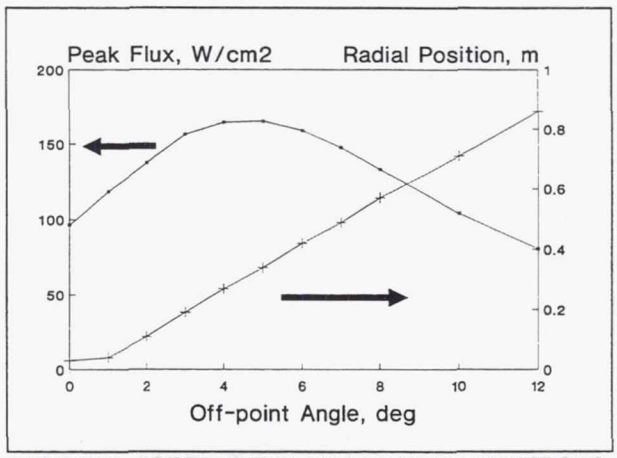

FIGURE 8. APERTURE PLANE PEAK FLUX VERSUS POINTING ERROR

REPORT DOCUMENTATION PAGE

Form Approved
OMB No. 0704-0188

1. AGENCY USE ONLY (*Leave blank*)	2. REPORT DATE	3. REPORT TYPE AND DATES COVERED
	June 1995	Technical Memorandum

4. TITLE AND SUBTITLE
Analysis of Solar Receiver Flux Distributions for US/Russian Solar Dynamic System Demonstration on the MIR Space Station

5. FUNDING NUMBERS
WU-547-10-11

6. AUTHOR(S)
Thomas W. Kerslake and James Fincannon

7. PERFORMING ORGANIZATION NAME(S) AND ADDRESS(ES)
National Aeronautics and Space Administration
Lewis Research Center
Cleveland, Ohio 44135-3191

8. PERFORMING ORGANIZATION REPORT NUMBER
E-9660

9. SPONSORING/MONITORING AGENCY NAME(S) AND ADDRESS(ES)
National Aeronautics and Space Administration
Washington, D.C. 20546-0001

10. SPONSORING/MONITORING AGENCY REPORT NUMBER
NASA TM-106933
IECEC-95-136

11. SUPPLEMENTARY NOTES
Prepared for the 30th Intersociety Energy Conversion Engineering Conference cosponsored by ASME, IEEE, AICHE, ANS, ACS AND AIAA, Orlando, Florida, July 31-August 1, 1995. Responsible person, Thomas W. Kerslake, organization code 6920, (216) 433-5373.

12a. DISTRIBUTION/AVAILABILITY STATEMENT
Unclassified - Unlimited
Subject Category 20

This publication is available from the NASA Center for Aerospace Information, (301) 621-0390.

12b. DISTRIBUTION CODE

13. ABSTRACT (*Maximum 200 words*)

The United States and Russia have agreed to jointly develop a solar dynamic (SD) system for flight demonstration on the Russian MIR space station starting in late 1997. Two important components of this SD system are the solar concentrator and heat receiver provided by Russia and the U.S., respectively. This paper describes optical analysis of the concentrator and solar flux predictions on target receiver surfaces. The optical analysis is performed using the code CIRCE2. These analyses account for finite sun size with limb darkening, concentrator surface slope and position errors, concentrator petal thermal deformation, gaps between petals, and the shading effect of the receiver support struts. The receiver spatial flux distributions are then combined with concentrator shadowing predictions. Geometric shadowing patterns are traced from the concentrator to the target receiver surfaces. These patterns vary with time depending on the chosen MIR flight attitude and orbital mechanics of the MIR spacecraft. The resulting predictions provide spatial and temporal receiver flux distributions for any specified mission profile. The impact these flux distributions have on receiver design and control of the Brayton engine are discussed.

14. SUBJECT TERMS
Space stations; Solar dynamic power systems; solar collectors; Performance prediction; Concentrators

15. NUMBER OF PAGES
08

16. PRICE CODE
A02

17. SECURITY CLASSIFICATION OF REPORT	18. SECURITY CLASSIFICATION OF THIS PAGE	19. SECURITY CLASSIFICATION OF ABSTRACT	20. LIMITATION OF ABSTRACT
Unclassified	Unclassified	Unclassified	